Surface & Coatings Technology 476 (2024) 130304

Contents lists available at ScienceDirect

Surface & Coatings Technology

journal homepage: www.elsevier.com/locate/surfcoat

Brushite/hydroxyapatite coatings on H_2SO_4 passivated 316LSS by electrodeposition: *In vitro* corrosion and anti-inflammatory activity

Gabriela Morais da Costa [a,b,*], Gustavo Oliveira Everton [c], Gustavo Oliva Amaral [d], Glauber Cruz [a], Anupama Ghosh [e], Maria Eliziane Pires de Souza [a]

[a] Laboratory of Materials and Manufacturing Processes, Department of Mechanical Engineering, Federal University of Maranhão, UFMA, 65080-805 São Luís, MA, Brazil
[b] Laboratory of Biomaterials and Tissue Engineering, Graduate Program in Biomedical Engineering, Federal University of ABC, UFABC, São Bernardo do Campo, SP, Brazil
[c] Laboratory of Research and Application of Essential Oils, Federal University of Maranhão, UFMA, 65080-805 São Luís, MA, Brazil
[d] Departament of Biosciences, Federal University of São Paulo, UNIFESP, 11015-020 Santos, SP, Brazil
[e] Department of Chemical and Materials Engineering, Pontifical Catholic University of Rio de Janeiro, PUC-Rio, 22451-900 Rio de Janeiro, RJ, Brazil

ARTICLE INFO

Keywords:
316L stainless steel
Surface modification
CaP-based coatings
Electrodeposition
EIS

ABSTRACT

This study evaluated the corrosion behavior and anti-inflammatory activity of brushite (BS or DCPD, $CaHPO_4{\cdot}H_2O$)/hydroxyapatite (HAp, $Ca_{10}(PO_4)_6(OH)_2$) coating on sulfuric acid (H_2SO_4) treated 316L stainless steel (SS). The coating was applied using the electrodeposition process on untreated and H_2SO_4 passivated 316L SS surface. The obtained samples were characterized by X-ray diffraction (XRD), Fourier transform infrared spectroscopy (FTIR), scanning electron microscopy (SEM) and X-ray energy dispersive spectroscopy (EDS) to obtain crystal and electronic structure as well as morphological and compositional information of the coated 316L SS. Electrochemical impedance spectroscopy (EIS) tests were performed in 0.9 % sodium chloride (NaCl) solution and compared with the pristine (P316L), H_2SO_4 treated (T316L), untreated/BS/HAp coated (BHP316L) and treated/BS/HAp coated (BHT316L) 316L SS specimens. The anti-inflammatory activity was carried out for the coated samples by the protein denaturation method. The results showed that the BS/HAp coating on H_2SO_4 treated 316L SS (hereafter, denoted as BHT316L) were susceptible to corrosion attack against 0.9 % NaCl solution. Additionally, the anti-inflammatory activity of the BHT316L was found to be lower compared to control (sodium diclofenac), indicating that particular concern should be given to H_2SO_4 treated 316L SS as the corrosion products formed by this surface modification may cause harmful effects in the human physiological environment.

1. Introduction

316L stainless steel (316L SS) is one of the most used materials for orthopedic applications, owing to its high mechanical strength, corrosion resistance properties and low cost [1,2]. However, when implanted in the human body for a prolonged period, pitting and crevice corrosion becomes a constant problem faced by this metal. The performance and integrity of the implant are compromised by high levels of Cl^- ions in human body fluid, a pH of around 7.4, and body temperature ranging from 36.7 to 37.2 °C, which is considered a severe environment for this particular metal [3]. In addition, a recent study showed that inorganic (H_2O_2) and organic (albumin) species combined lead to a large dissolution of the Fe and Cr oxides in peri-implanted environments [4]. Likewise, Cadosch et al. [5] reported findings from 316L SS biocorrosion by osteoclasts (OC), where the authors observed that mature OC presents ability to corrode the surface of the metallic implant and the released metal ions induce inflammatory reactions, which may lead to unsatisfactory biocompatibility and acceptance of the implant by the human body [5]. To avoid the deleterious effects caused by corrosion products on normal bone formation, biocompatible coatings have been used to resist the dissolution of metal ions improving biocorrosion resistance [6–8] and promote the formation of new bone tissue [6].

Hydroxyapatite [HAp, $Ca_{10}(PO_4)_6(OH)_2$] is a ceramic biomaterial whose main constituents are calcium and phosphorus, in a molar ratio of

* Corresponding author at: Laboratory of Materials and Manufacturing Processes, Department of Mechanical Engineering, Federal University of Maranhão, UFMA, 65080-805 São Luís, MA, Brazil.
E-mail address: gabriela.morais@ufabc.edu.com.br (G.M. Costa).

https://doi.org/10.1016/j.surfcoat.2023.130304
Received 27 September 2023; Received in revised form 23 November 2023; Accepted 11 December 2023
Available online 13 December 2023

1.67. HAp shows the greatest stability in the physiological environment (pH ≈ 7), whereas other calcium phosphates such as monetite (DCPA, $CaHPO_4$), dicalcium phosphate dihydrate or brushite (DCPD or BS, $CaHPO_4{\cdot}2H_2O$) and octacalcium phosphate (OCP, $Ca_8(HPO_4)_2(PO_4)_4{\cdot}5H_2O$) are more stable in acidic conditions [9]. Once introduced into the body, these acidic phosphates tend to transform into HAp [9]. The BS, in particular, due to its high solubility in physiological media, can dissolve and possibly provide increased levels of calcium and phosphate ions nearby the tissue-implant interface [10]. HAp exhibits an excellent biological activity, allowing the human cell to remain viable, grow and perform its functions properly, besides offering bioactivity and stimulating the formation of apatite (phosphate group of minerals) [11,12]. Another factor that favors the ingrowth of new bone tissue is its macro-porosity, in other words, having pores with diameters >100 μm and the interconnectivity of HAp pores [13]. Also, according to literature [14], the application of bioactive calcium phosphate (CaP) coatings, such as hydroxyapatite, could provide higher amounts of Ca^{2+} and PO_4^{3-} in the early stages of implantation, implying a smaller amount of soluble biocompatible hydroxyapatite to be achieved. Studies confirmed that CaP-based coatings promote osteoblasts' fixation, proliferation, and differentiation [15]. However, due to the poor adhesion of the hydroxyapatite coating to the metallic substrate, it degrades over time, making the metal alloy susceptible to corrosion [16].

The main approach to preventing metallic corrosion and enhancing the adhesion of CaP coatings on implants has been surface modification before the coating/deposition [16]. Among numerous methods for surface modification, chemical treatments such as sulfuric acid passivation of 316L SS have demonstrated that an H_2SO_4 environment ensures a passive oxide layer, rich in molybdenum and chromium, which are responsible for the localized corrosion resistance of 316L SS and improvement of the bond strength of bioceramic coatings [6,17]. Most literature on hydroxyapatite coatings on H_2SO_4-treated 316L SS surface has generally focused on electrochemical response in physiological solutions [6,17,18]. For example, Parsapour and coworkers [18] found that H_2SO_4-treated and HAp-coated 316L SS improve corrosion behavior of the metallic implant. However, they did not investigate if the dissolution of metal ions from this passive layer through the hydroxyapatite coating can lead to unwanted biological reactions such as inflammatory responses. The applicability of biomaterials in clinical practice depends on fulfilling many requirements such as the absence of an inflammatory response by the biomaterial to ensure the safety and effectiveness of the patient [19] and thus demand a better and thorough study.

Different research has been carried out regarding the electrodeposition of hydroxyapatite, such as the work of Thanh et al. [20] who evaluated the influence of some parameters such as precursor concentration and temperature on the characteristics of the coating formed. Gopi et al. [21] studied the effects of galvanostatic direct and pulsed current electrodeposition methods on hydroxyapatite coatings in terms of morphology and corrosion. Although there is literature establishing the relationship between the morphology, composition and corrosion resistance of hydroxyapatite coatings obtained by electrodeposition, there are still few studies relating the effects of passivating the surface of 316L SS with H_2SO_4 and the corrosive behavior and inflammatory action of electrodeposited coatings. Therefore, the present work aims to investigate the corrosion properties of electrodeposited hydroxyapatite/brushite coatings on an intermediate layer obtained by H_2SO_4 treatment on the 316L SS surface and the possibility of the metallic ions from the oxide layer stimulate the protein denaturation, which is responsible for the inflammatory processes. The BS/Hap coatings produced here were characterized for the untreated and H_2SO_4-treated 316L SS surface by Fourier transform infrared spectroscopy (FT-IR), X-ray diffractometry (XRD), scanning electron microscopy (SEM), and energy-dispersive X-ray analysis (EDS). Electrochemical impedance spectroscopy assay was performed in 0.9 % NaCl (sodium chloride) solution (pH = 6.0) at room temperature. Finally, the anti-inflammatory activity of the coatings was studied by the protein denaturation method.

2. Materials and methods

2.1. 316L SS substrate treatment

316L SS sheet (Cr: 16.5 %, Ni: 10 %, Mn: 2 %, Mo: 2 %, Si: 0.75 %, N: 0.10 %, P: 0.045 %, S: 0.015 %, C: 0.03 % in weight), obtained from Aperam South America (Belo Horizonte, Brazil), was cut in rectangular plates (20 mm × 20 mm × 1 mm), and used as substrate material in this work. Before electrodeposition, substrates were ground polished using wet SiC papers (grit numbers P1200, P1500, and P2000) and abraded with 1 μm alumina suspension to achieve a mirror-like surface. Subsequently, these plates were ultrasonically cleaned with distilled water, 99.5 % ethanol and acetone, for 10 min each and finally dried at room temperature.

2.2. Surface treatment process by H_2SO_4

For H_2SO_4 treatment, some 316L SS samples were immersed in 1 M sulfuric acid (H_2SO_4, Química Moderna, Brazil) solution at 70 °C for 15 min. These H_2SO_4-treated samples were washed in distilled water to remove the excess of sulfuric acid. These H_2SO_4-treated samples were submitted to electrochemical deposition freshly after this treatment.

2.3. Electrodeposition of CaP coatings on 316L SS

The electrodeposition procedure consisted of a three-electrode system with 316L SS substrate (untreated and H_2SO_4-treated) as working electrode (cathode), platinum plate as counter-electrode (anode), and saturated calomel electrode (SCE) as a reference electrode immersed into aqueous solutions containing 0.42 M calcium nitrate tetrahydrate ($Ca(NO_3)_2{\cdot}4H_2O$, ISOFAR, Brazil) and 0.25 M ammonium dihydrogen phosphate ($NH_4H_2PO_4$, ISOFAR, Brazil). The concentration of the electrolytes were chosen to have a Ca/P molar ratio of 1.67, in order to expect the electrodeposition of HAp phase on the 316L SS surface [22]. The initial pH of the bath was about 4.5, measured at 25 °C. The solution was mechanically stirred at a velocity of 120 rpm to maintain a uniform concentration of the electrolyte throughout. The deposition was carried out at room temperature to prevent evaporation issues. Electrodeposition was performed using Autolab PGSTAT302N potentiostat (Metrohm, United States) using the potentiostatic technique (chronoamperometry) at a constant potential of −2 V for 30 min. Subsequently, the samples were removed from the electrolytic solution and gently washed in distilled water before using for further studies. After the deposition the coated samples were dried at 60 °C in an oven for 30 min.

2.4. Surface characterization

XRD test was performed with a Bruker (Model D8 Advance, United States) diffractometer to identify the chemical phase of the CaP coatings using CuK_α radiation (λ = 0.154056 nm) with a scan rate of 1° min^{-1}. The average crystal size (D) of CaP was calculated by Scherrer Formula (Eq. (1)) and the crystallinity index (X_c) (Eq. (2)) of CaP on the metal surface was evaluated according to the described method [20,23].

$$D = \frac{0.9\,\lambda}{\beta cos\theta} \tag{1}$$

$$X_c = \frac{Area\ of\ all\ the\ crystalline\ peaks}{Area\ of\ all\ the\ crystalline\ and\ amorphous\ peaks} \tag{2}$$

FTIR spectra were recorded in an IR-Prestige-21 Fourier transform spectrophotometer (Shimadzu Corporation, Japan) to confirm the presence of functional groups that indicate the deposition of CaP on the 316L SS surface. The scanning range was from 4000 to 400 cm^{-1}, in the transmittance mode, by using the KBr pellet method, which consisted of scratched off the material from the electrode and mixed with KBr.

The morphology of the electrodeposited CaP coating was

characterized using a Quanta 450 FEG microscope (FEI, United States) operated at 20 kV. The microscope was equipped with an X-Ray detector model 150 from Oxford, which was used to perform energy dispersive X-ray spectroscopy (EDS) in order to measure the elemental composition and obtain the Ca/P ratio of precipitated calcium phosphate phase for each sample. To analyze the H_2SO_4 treated 316L SS and evaluate the growth of the oxide layer on its surface, SEM analysis was conducted using a Hitachi model TM3000 microscope operated at 15 kV. The microscope was equipped with an X-Ray detector model SwiftED3000, which allowed for the characterization of the morphology and composition of the oxide layer. Cross-sectional images of the coatings were obtained using 20 × 20 mm substrates, and subsequent examination was conducted through scanning electron microscopy (SEM, JEOL, JSM 7100FT).

Sample surfaces were examined using a profilometer (Dektak XT from Bruker) to measure the substrate roughness. A 5 mm scan was employed for coated samples, whereas a 1 mm scan was used for uncoated samples.

2.5. Electrochemical impedance spectroscopy studies

Electrochemical impedance spectroscopy (EIS) of pristine (P316L), H_2SO_4 treated (T316L), untreated/BS/HAp coated (BHP316L) and treated/BS/HAp coated (BHT316L) 316L SS samples were performed using a 0.9 % sodium chloride solution as an electrolytic media to study the corrosion behavior. Assays were performed at room temperature (~25 °C), and the 0.9 % NaCl solution was renewed each experiment to keep its concentration. The configuration implemented for the study was a three-electrode cell fitted with KCl-saturated Ag/AgCl electrode as the reference electrode, platinum wire as the counter electrode, pristine and coated 316L stainless steel as the working electrode, all connected to an Autolab PGSTAT302N potentiostat (Metrohm, United States) controlled by a computer using Nova 2.1.5 software. The measurements for the electrochemical impedance spectroscopy (EIS) test were achieved in the frequency range from 10 kHz to 100 mHz, with a small AC perturbation of 10 mV and 15 points per frequency decade at the open circuit potential (OCP). Impedance spectra were represented in both Nyquist and Bode plots. The electrode potential was allowed to stabilize 30 min before starting each run. To ensure the reproducibility of the results, each experimental condition was performed two times using independent samples (n = 2). The EIS plots were fitted using an electrical equivalent circuit (EEC) modeling by Nova 2.1.5 software, and the quality of the adjustment was considered excellent for values $\chi^2 < 10^{-3}$ and percentage error <5 % for each element of the circuit. Furthermore, to ensure a good agreement between simulated and experimental data, pure capacitors were replaced by constant phase elements (CPE) [24].

2.6. Anti-inflammatory activity

The anti-inflammatory activity was evaluated according to the protein denaturation method proposed by Jenifer et al. [25] with slight modifications. For obtaining the reaction mixture (4 mL), 0.02 g of the coatings were scraped off from the surface of the samples and dissolved in 10 mL of phosphate buffer saline (PBS, pH 6.4), constituting the stock solution, which was homogenized for 6 min in an ultrasonic bath. Then, different concentrations (200, 400, 600, 800, and 1000 μg mL^{-1}) were removed from the stock solution and made up to 2 mL with PBS, added to a test tube containing 2 mL of 10 % egg albumin (from fresh hen's egg), and incubated at 37 °C for 10 min. Denaturation was induced by keeping the reaction mixture at 60 °C in a water bath for 10 min. After cooling, absorbance was measured at 660 nm by using doubly distilled water as blank through a BEL PHOTONICS UV–Vis spectrophotometer (model V-M5, Brazil). Sodium diclofenac (200, 400, 600, 800, and 1000 μg mL^{-1}) was used as a standard solution and the absorbance was determined. Each analysis was carried out in duplicate (n = 1) and the average was presented as a result. The percentage inhibition of protein denaturation was calculated using Eq. (3):

$$\%inhibition = (A_t - A_c)/A_c \times 100 \quad (3)$$

where, A_t = test sample absorbance; A_c = control absorbance. Results were represented graphically along with standard deviation.

3. Results and discussion

The physicochemical properties of pristine 316L SS changes on H_2SO_4 treatment, and when subjected to CaP electrodeposition, these two samples behave slightly different from each other, and this has an impact on their corrosion resistance properties and anti-inflammatory activity. To thoroughly understand these changes, for comprehensive purposes these samples were designated with simpler names, presented in Table 1.

Table 2 presents the roughness analysis, as measured by the DekTak XT profilometer, at four different points of each sample. The results reveal that the roughness for P316L samples is approximately 0.014 μm after polishing by alumina solution. After treatment in sulfuric acid, the roughness of the T316L surface increases to about 0.038 μm, which indicates the growth of an oxide layer. The high roughness of the BHP316L sample, measured in the scan profile, is corroborated by the irregular topography identified in the SEM images (Fig. 3c). The high standard deviation associated with this sample confirms the irregularity of the surface.

Fig. 1 displays the XRD patterns of the CaP coatings that were deposited on pristine 316L SS and H_2SO_4-treated 316L SS. For comparison, the XRD of the 316L SS substrate is also included. According to XRD patterns, the primary phase of the coatings deposited in both the samples is dicalcium phosphate dihydrate (brushite, BS, $CaHPO_4{\cdot}2H_2O$), as confirmed by both XRD and FTIR analysis. Hydroxyapatite (HAp, $Ca_{10}(PO_4)_6(OH)_2$) is also present as a secondary phase.

The X-ray diffraction pattern of the BHP316L exhibits broad peaks, which suggest a smaller size of the crystallite/particle in this sample (corroborated by Table 3) [26,27]. Common HAp peaks can be observed at 2θ ≈ 26.3°, 31.7°, 32,9°, 39.8° which correspond to the (002), (211), (300) and (130) planes, respectively [1]. The BS phase was also detected in the peaks at 2θ ≈ 11.9° (020), 21.3° (121), 29.6° (041) and 34.5° ($\bar{2}21$) [28]. Surface BS precipitation may be aligned with local pH conditions [29]; upon establishing that brushite deposition exhibits kinetic stability in acidic solutions (pH range 2–6.5) while stoichiometric HAp is stable over the neutral and basic pH range [9,30]. The peaks at 2θ ≈ 44.2°, 51.3°, and 75.1° (austenite γ) were assigned as the (111), (200), and (220) planes of 316L SS surface and its oxides [31,32]. The BHT316L sample shows narrower peaks, suggesting that H_2SO_4 treatment influenced the crystallinity and grain size of the coating.

Table 3 shows the crystallinity index and crystallite size of BHP316L and BHT316L coatings. The crystallinity degrees are 73.5 and 51.5 % for BHP316L and BHT316L samples, respectively. It can be noticed that H_2SO_4 surface treatment decreases the crystallinity index of calcium phosphate coatings, which can be seen by the weak peak intensities.

In addition, using Eq. (1), the prominent peak of HAp and BS showed crystallite size of 23.8 nm and 22.1 nm, respectively, in the case of BHP316L sample. Similarly, for the BHT316L sample, the dominant peak of HAp and BS exhibited crystallite sizes of 60.8 nm and 59.7 nm, respectively. Generally, particles with smaller crystallite size tend to have a higher specific surface area, which can increase the adsorption of

Table 1
Applied treatment and designated names of the samples.

Treatments	Samples name
Pristine 316L SS	P316L
H_2SO_4 treated 316L SS	T316L
CaP coated pristine 316L SS	BHP316L
CaP coated H_2SO_4 treated 316L SS	BHT316L

Table 2
Mean roughness values and standard deviation of the surface samples of each group.

Sample	Roughness (μm)
P316L	0.014 ± 0.002
T316L	0.038 ± 0.008
BHP316L	13.340 ± 1.544
BHT316L	3.940 ± 0.342

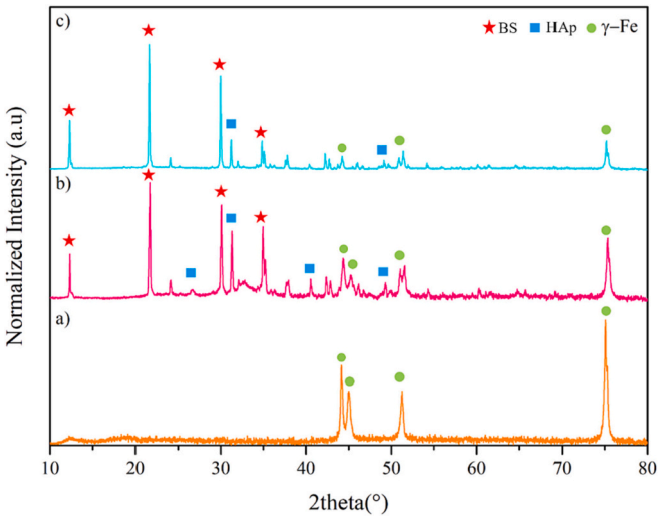

Fig. 1. XRD spectra: a) P316L, b) BHP316L, and c) BHT316L samples.

Table 3
The crystallinity index (%) and crystallite size (nm) derived from XRD analysis for the different CaP conditions.

	BHP316L		BHT316L	
CaP phase	HAp	BS	HAp	BS
Crystallite size (nm)	23.8	22.1	60.8	59.7
Crystallinity index (%)	73.5		51.5	

proteins and other molecules that promote cell adhesion and proliferation. On the other hand, particles with larger crystallite size can be more efficient in providing calcium and phosphate ions to the culture medium [33]. The increase in crystallite size of the BHT316L sample might be due to the chemical modification by H_2SO_4, once the surface of the substrate became more activated for crystal growing. Previous studies reported that HAp nanoparticles 20 nm in size presented the desired result in promoting cell proliferation and cellular activity, and inhibiting cell apoptosis [34–36].

FTIR spectra of the BHP316L and BHT316L coatings are shown in Fig. 2. Therefore, FTIR confirms both calcium phosphate phases in the powder's samples. Table 4 shows the wavenumbers of the measured IR spectra of both samples. An evident characteristic of BS is the presence of two strong doublets in the O—H stretching region, one composed of components at 3585 and 3437 cm^{-1}, and the other consisting of components at 3284 and 3107 cm^{-1}. These doublets are associated with the two different types of water molecules present in the unit cell [37]. The brushite phase also displayed peaks at 1647 cm^{-1}, indicating bending motion of H_2O molecules, 1223 cm^{-1}, suggesting in-plane bending of O—H bonds, and 798 cm^{-1}, representing oscillating motion of H_2O molecules [38]. The peaks corresponding to PO stretching in both coated samples were detected at wavenumbers of 1138, 1067 and 985 cm^{-1} [38]. The band at 870 cm^{-1} may be attributed to HPO_4^{2-} or carbonate (CO_3^{2-}), which can be also associated with BS and HAp phase, respectively [35,39]. The characteristic absorption bands of HAp are not

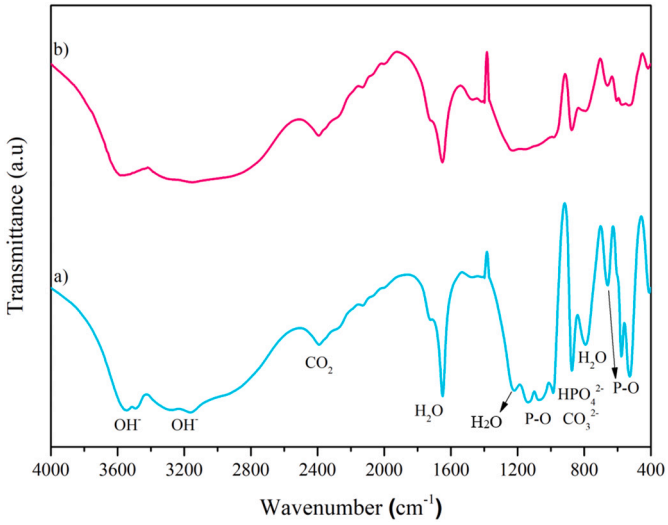

Fig. 2. FT-IR spectra: a) BHP316L and b) BHT316L coatings.

Table 4
A summary of wavenumber assignments of FTIR spectra.

FTIR KBr	Assignment
3900–2500 cm^{-1}	OH^- stretching
2388 cm^{-1}	CO_2 asymmetric stretching
1647 cm^{-1}	H_2O bending
1223 cm^{-1}	OH in-plane bending
1138 cm^{-1}	P-O stretching mode in PO_4
1067 cm^{-1}	P-O stretching mode in PO_4
985 cm^{-1}	P-O stretching mode in PO_4
874 cm^{-1}	P-OH stretching mode in HPO_4^{2-} CO_3^{2-} vibration
798 cm^{-1}	H_2O oscillating motion
659 cm^{-1}	PO_4^{3-} bending vibrational mode (υ_4)
579 cm^{-1}	P-O bending vibrational mode
531 cm^{-1}	P-O bending vibrational mode

clearly noticeable in all FTIR spectra, once the corresponding stretching vibration to PO_4^{3-} ions at 605–560 cm^{-1} (υ_4), 963 cm^{-1} (υ_1), and 1045 cm^{-1} (υ_3) might be overlapped by absorption peaks of BS [39,40]. The BHT316L sample exhibited a broad band within the 1200–1000 cm^{-1} region, which lacked visibly distinct peaks and displayed reduced intensity. These observations suggest a limited degree of crystallinity, which was confirmed by XRD analysis.

The SEM morphology of the P316L, T316L, BHP316L and BHT316L samples are displayed in Fig. 3. On the polished surface of P316L (Fig. 3a), some impurities are observed, which may be associated with alumina suspension. In addition, a few scratches are present on P316L substrates due to the manual polishing. As for T316L sample (Fig. 3b), it is possible to see small black spots on its surface, which may be corrosion points associated with acid attack. The deposits of BHP316L (Fig. 3c–d) have plate-like crystals (flakes). SEM images from BHP316L also show that the coating contains irregular thin plate-like crystals with varying sizes, which affects the uniformity of the coating. The production of H_2 bubbles in the vicinity of the electrode is correlated to the non-uniformity of HAp deposition onto the surface [41]. Although visual analysis reveals the presence of some pores and small cracks on the surface and in cross-sectional areas (Fig. 3g) of this sample, it is observable that the coating exhibits a denser layer. This improved density contributes to the coating's effectiveness as a semi-mechanical barrier, thereby mitigating the corrosive behavior of 316L SS [42]. The BS/HAp coating deposited on H_2SO_4-treated 316L SS (Fig. 3e–f) reveals a slight difference from the shape of BHP316L, exhibiting coating plate-like crystals more compact, regular flake sizes, and

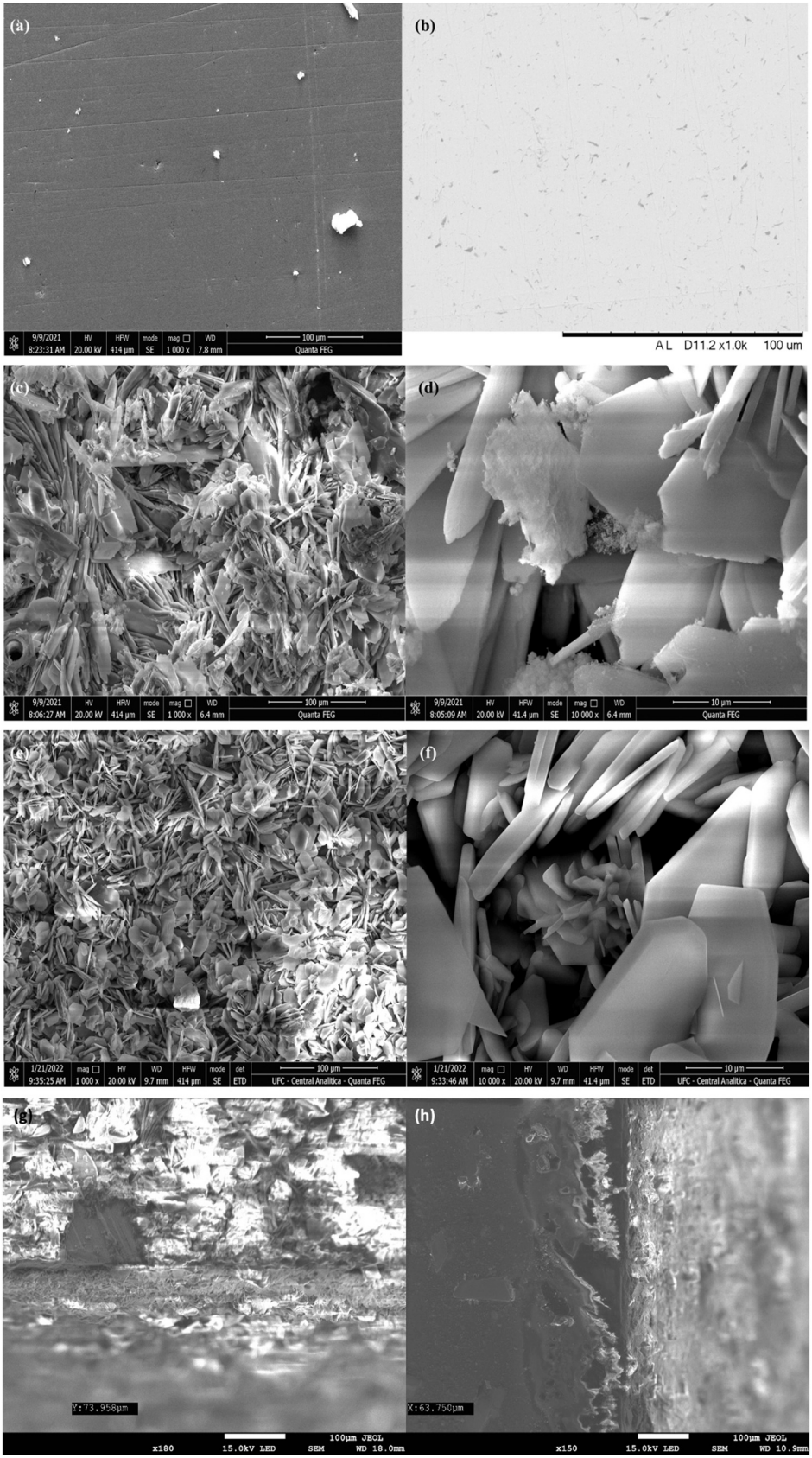

Fig. 3. SEM micrographs of the top view: a) P316L, b) T316L, c) BHP316L with a magnification of 1000×, d) BHP316L with a magnification of 10,000×, e) BHT316L with a magnification of 1000×, f) BHT316L with a magnification of 10,000×, and cross sectional view of g) BHP316L, and h) BHT316L samples.

uniformly distributed.

Micrographs of the cross sections of samples BHP316L and BHT316L are presented in Fig. 3g and h, respectively. It is noted that although the BHP316L coating appears to be relatively dense, some surface microcracks are discernible. Measurement in three distinct regions of this sample reveals a non-uniform layer deposit with an average thickness of 70.56 ± 3.61 μm. The presence of these microcracks suggests a more pronounced interfacial debonding compared to sample BHT316L.

When examining the cross section of BHT316L, it is possible to identify a more homogeneous layer, with an average thickness of 62.41 ± 4.82 μm and the absence of detectable cracks. Therefore, it is reasonable to infer that the chemical modification with sulfuric acid contributed to a better adhesion to the 316L SS substrate, indicating a stronger interfacial bond between the substrate and the coating [43].

This analysis highlights that although the calcium phosphate coating alone may not act as an effective barrier to the release of metal ions into the body, its thickness plays a crucial role [44]. The results indicate that an increase in coating thickness is associated with a significant improvement in corrosion resistance and reduced ion release, potentially minimizing tissue inflammatory responses and other adverse histopathological reactions [45–47].

The results of the EDS analysis of BHP316L and BHT316L are shown in Figs. 4 and 5. The theoretical stoichiometric molar ratio of calcium to phosphorus (Ca/P) in HAp is 1.67. Ca/P mass ratio of BHP316L is 1.61 while for BHT316L is 1.54. The Ca/P result of BHP316L is in agreement with the range (Ca/P ratio from 1.59 to 1.86) found in the literature for the hydroxyapatite phase but suggests the formation of a calcium deficient HAp (CDHAp) [9,48]. On the other hand, the Ca/P values did not correspond to the stoichiometric molar ratio of brushite (BS), which is equal to 1, but according to Blanda et al. [2], this does not guarantee deposits of pure HAp. The Ca/P ratio also corresponds to thick and homogeneous calcium phosphate coatings [49]. Then, BHP316L presents a thicker coating while BHT316L shows the thinnest, and this difference in thickness was discernible to the naked eye after the electrodeposition process. The EDS data from BHP316L (Fig. 4) shows the HAp elements (Ca, P and O) and some traces of the elements belonging to the 316L SS substrate, indicating that the surface presents a dense and continuous coating, with occasional exposure of the substrate below, which is reflected in the elemental mapping of the elements presented in the substrate, especially Fe. From EDS mapping shown in Figs. 4 and 5, the Ca (27.4 wt% for BHP316L and 26.1 wt% for BHT316L) and P element (17.0 wt% for BHP316L and 16.9 wt% for BHT316L) is distributed overall 316L SS substrate of both coatings. According to Cao et al. [50], phosphorus plays an important role in the Ca/P ratio, which influences osteogenic properties significantly. Fig. 5 reveals a high presence of Fe, Cr, Ni, and especially O elements on the surface of BHT316L, suggesting the formation of Cr_2O_3, Fe_2O_3, and NiO on the passive layer [51]. The elemental composition of BHP316L and BHT316L in wt% are given in Figs. 4i and 5i, respectively. From the table values, the enrichment of Mo does not occur in BHT316L. Decreasing the Mo oxide concentration and increasing the Fe concentration in the metallic surface may be associated with the low corrosion resistance found in the EIS studies for this coating (Fig. 6). The composition of the T316L sample was analyzed and is presented in the Supplementary data (Table S1). Based on the composition of the 316L SS given by the manufacturer, it appears that the chemical modification using sulfuric acid 0.1 M at 70 °C for 15 min had a significant effect on the surface of the 316L SS sample. The results indicate a change in the elemental composition of the surface, particularly in the concentrations of C, Si, and Fe, while the concentrations of Cr remained relatively stable. The significant increase in the concentration of C on the surface suggests the formation of a carbon-rich layer, likely due to the preferential removal of the oxide layer during the acid treatment. The increase in Fe concentration may be attributed to the formation of iron sulfate compounds during the reaction. The decrease in Ni concentration could be a result of its dissolution in the acid solution.

From the literature, the constitution of the calcium phosphate coating is influenced by the pH adjacent to the cathode, which is linked to the current intensity determined by the generator. However, different experimental factors, such as electrolyte temperature and ionic concentrations, have the ability to modify the chemical composition of the coating [20,44,52].

In the electrochemical deposition technique, the application of a voltage of −2 V to the electrolyte results in the increased generation of hydroxyl ions (OH^-) and the evolution of hydrogen gas (H_2), as expressed by Eqs. (4)–(5) [2,42,53]:

$$2H_2O + 2e^- \rightarrow H_2 + 2OH^- \quad (4)$$

$$O_2 + 2H_2O + 4e^- \rightarrow 4OH^- \quad (5)$$

The production of OH^- ions through Eqs. (4) and (5) induces an increase in pH at the cathode/electrolyte interface [2]. This local increase in pH shifts the dissociation equilibrium of $H_2PO_4^-$ ions towards HPO_4^{2-}

$$H_2PO_4^- + OH^- \leftrightarrow HPO_4^{2-} + H_2O \quad (6)$$

The progression of this reaction results in the deposition of a brushite-type deposit, as expressed by the equation

$$Ca^{2+} + HPO_4^{2-} + 2H_2O \rightarrow CaHPO_4 \bullet 2H_2O \quad (7)$$

According to this mechanism, a layer of calcium phosphate (BS) is formed on the surface of the substrate. The formation of a compact and uniform layer, being electrically insulating, makes electrochemical reactions difficult. However, if the BS layer formed is porous and/or non-uniform, Eqs. (4) and (5) may persist at some points on the electrode, causing an additional increase in pH [2,42,53].

At places where the concentration of hydroxyl ions increases, acid phosphates are completely converted into phosphates, following equilibrium

$$HPO_4^{2-} + OH^- \leftrightarrow PO_4^{3-} + H_2O \quad (8)$$

As Eqs. (4) and (5) raise the interfacial pH to values >12, the presence of PO_4^{3-} can be inferred. Consequently, as stated by Bir et al. [44], hydroxyapatite phosphate (HAp) can precipitate

$$10Ca^{2+} + 6PO_4^{3-} + 2OH^- \rightarrow Ca_{10}(PO_4)_6(OH)_2 \quad (9)$$

The outcome of the electrochemical process is the deposition of calcium phosphate (BS/HAp) on the surface of SS 316L.

Fig. 6 shows the Nyquist and Bode plots of the P316L, BHP316L, and BHT316L samples in 0.9 % NaCl solution at 25 °C. For the pristine sample, the polarization resistance R_p value is observed as 1.21×10^4 Ω. Compared with P316L, the T316L obtained a lower polarization resistance, suggesting that the acid treatment caused damage or alteration to the oxide layer, which could have negatively impacted its ability to protect the steel against corrosion but can be good to activate the good HAp/BS adhesion. This result also contributed to a lower R_p value (1.05×10^4 Ω) of the BHT316L sample, while a maximum value R_p of 1.76×10^4 Ω was obtained for the BHP316L sample. Ahmadi and Afshar [54] reported that the high resistance is related to the diameter of the semicircle, a large diameter prevents the release of ions from the substrate surface and penetration of Cl^- ions on the substrate surface. The same authors also mentioned that a high corrosion resistance indicates crack-free coatings with good coverage over the substrate surface. In contrast, the BHT316L sample has the smallest semicircle diameter, which may indicate a surface attack by ions existing in the NaCl solution. As reported by Xu et al. [55], under non-oxidizing environments such as boiling dilute sulfuric acid solution where the passive oxide layer cannot be steadily passivated on the substrate, SS becomes prone to severe corrosion. Analyzing the curves in Fig. 6b obtained coatings present two-time constants: the first related to the reaction in the coating/electrolyte interface and the second to processes in the coating/substrate interface

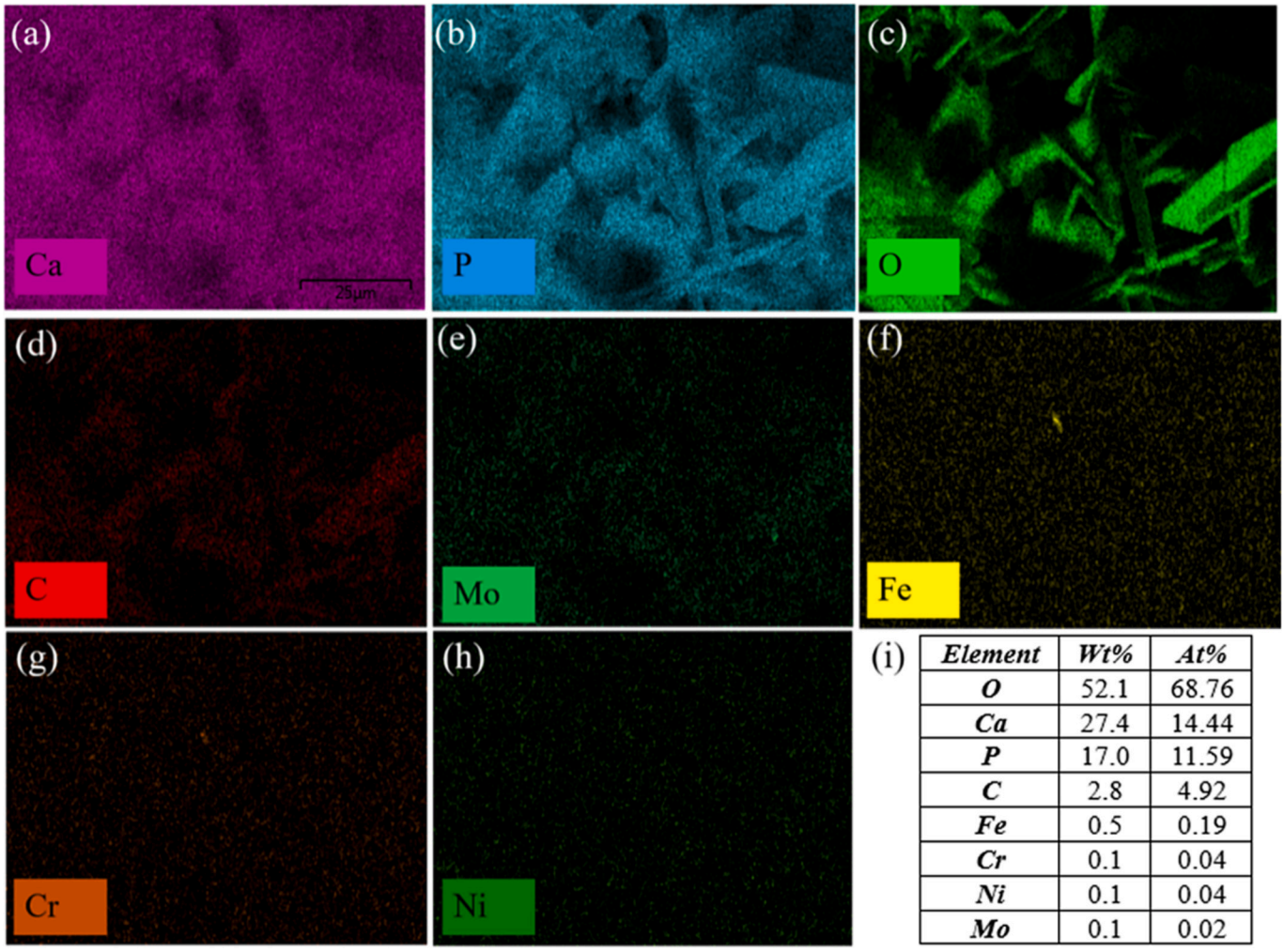

(i)

Element	Wt%	At%
O	52.1	68.76
Ca	27.4	14.44
P	17.0	11.59
C	2.8	4.92
Fe	0.5	0.19
Cr	0.1	0.04
Ni	0.1	0.04
Mo	0.1	0.02

Fig. 4. Elemental mapping analysis and the corresponding EDS spectra of the BHP316L specimen.

[56]. In the middle frequency range (10^0–10^2 Hz), the phase angle of BHP316L is around, presenting a nearly capacitive behavior (56), while the phase angle of BHT316L is lower than that found in pristine 316L SS. To summarize, these results demonstrate that the BHP316L is more corrosion-resistant in 0.9 % NaCl than BHT316L samples and reveal that the pretreatment of 316L SS specimen using 1 M H_2SO_4 solution has negatively changed the corrosion behavior of the 316L SS in 0.9 % NaCl. In other words, the acid treatment may have caused damage to the oxide layer, for example by creating cracks, pore, or defects, which could have compromised its ability to provide a reliable barrier against corrosion. Those defects can be seen in SEM (Fig. 3b) The formation of a new oxide layer on top of the damaged layer may not have been sufficient to repair the damage or restore the layer's protective properties. Additionally, the new oxide layer may have been less stable or of lower quality than the original layer, which could have contributed to the poor impedance (Table 5) of both samples pre-treated with H_2SO_4.

Nova 2.1.5 software was used to fit the equivalent circuit models concerning the acquired EIS data as shown in Fig. 6. The agreement between the experimental and modeled results is obtained with a 6 % average error. For the pristine 316L SS, the equivalent circuit model of $R_s(R_pQ_1)$ was used; where R_s corresponds to the resistance produced by the electrolyte, R_p represents the polarization resistance of the pristine metallic substrate produced against the electrolyte, and Q_1 or C_dl was electrical double-layer capacitance of implant/electrolyte interface. Same equivalent circuit was adopted to the T316L, once a model with $R_s(R_pQ_1(R_{coat}Q_{coat}))$ didn't provide a good fitting, suggesting a potential breakdown of the oxide layer during the chemical modification in H_2SO_4 solution at 70 °C (Fig. 6a). This breakdown can be attributed to an enhanced ionic diffusion and accelerated electrochemical kinetics, leading to a heightened corrosion rate and a consequent increase in oxide film dissolution. As a result of this process, the protective oxide layer becomes thinner and more porous, facilitating a substantial increase in the corrosion rate [57,58].

Fig. 3b corroborates this finding by revealing the presence of corrosion pits on the sample surface. These pits indicate the existence of a compromised oxide layer, rendering it incapable of providing effective corrosion protection [59]. In this context, the corrosion mechanism unfolds in two distinct steps: the cathodic and anodic reactions, outlining a multi-faceted process contributing to the deterioration of the 316L stainless steel surface. The cathodic reaction entails the formation of H_2O and H_2 [57,58]. The mechanism is elucidated by Eqs. (10)–(13) and illustrated by Fig. 7.

1. Reduction in hydrogen:

$$H^+ + 2e^- \rightarrow H_2 \quad (10)$$

2. Oxygen reduction:

$$O_2 + 2e^- + 4H^+ \rightarrow 2H_2O \quad (11)$$

$$O_2 + 2e^- + 2H^+ \rightarrow H_2O_2 \quad (12)$$

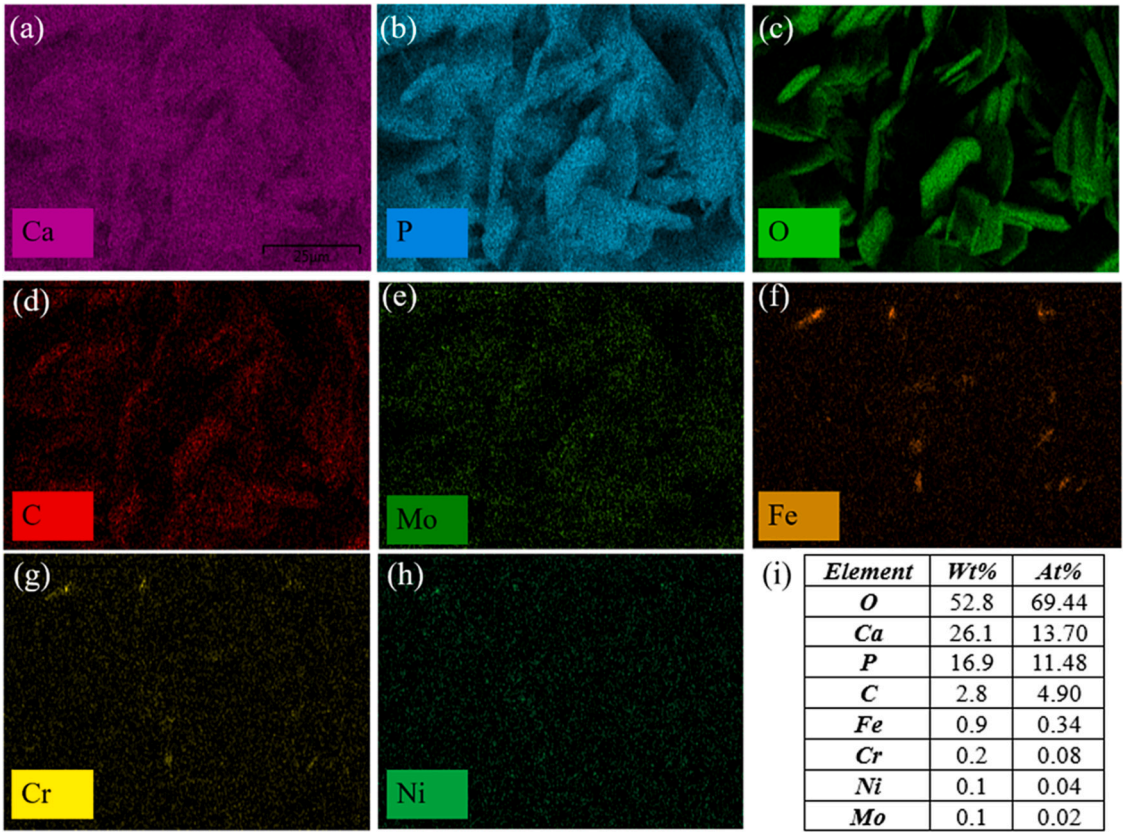

(i)

Element	Wt%	At%
O	52.8	69.44
Ca	26.1	13.70
P	16.9	11.48
C	2.8	4.90
Fe	0.9	0.34
Cr	0.2	0.08
Ni	0.1	0.04
Mo	0.1	0.02

Fig. 5. Elemental mapping analysis and the corresponding EDS spectra of the BHT316L specimen.

$$H_2O_2 + 2e^- + 2H^+ \rightarrow 2H_2O \quad (13)$$

The anodic reaction of 316L SS in sulfuric acid solution is given by the following equations:

$$(H_2O)_{ads} + SO_4^{2-} \leftrightarrow H_2O + (SO_4^{2-})_{ads} \quad (14)$$

$$Fe + SO_4^{2-} \leftrightarrow (FeSO_4^{2-})_{ads} \quad (15)$$

$$(FeSO_4^{2-})_{ads} \leftrightarrow (FeSO_4^{2-})_{ads} + 2e^- \quad (16)$$

$$(FeSO_4^{2-})_{ads} \leftrightarrow Fe^{2+} + SO_4^{2-} \quad (17)$$

In the presence of SO_4^{2-} anions, the evolution of the reaction described by Eq. (15) occurs accelerated on the metal surface. Therefore, the dissolution of the iron (anodic reaction) is predominantly governed by electro-dissolution of iron and diffusion of soluble complex $(FeSO_4^{2-})_{ads}$ in the NaCl solution [58]. Previous investigations, conducted by several researchers, have indicated that sulfur ions exert a deleterious influence of moderate to intense magnitude on steels when subjected to neutral or slightly alkaline NaCl solutions [59–61]. Another study noted that the absorption of SO_4^{2-} ions on the surface acts as an inhibitor of passive film growth, exacerbating its deficiency [58]. Additionally, the previously mentioned reaction culminates in local acidification, resulting in an increase in the dissolution rate of the passive layer [58]. The prevalence of the brushite phase in this sample is explained by the presence of a local acidic environment, since this phase demonstrates a propensity to deposit in acidic environments.

An equivalent circuit model of $R_s(R_pQ_1(R_{coat}Q_{coat}))$ was used to fit the spectra obtained for CaP coated on pristine and CaP coating on H_2SO_4 treated 316L SS samples. R_s corresponds to the solution resistance, R_{coat} corresponds to the charge-transfer resistance for the electrolytically deposited coatings, Q_{coat} indicates the electrical double-layer capacitance created between the coating/electrolyte interface, R_p represents the polarization resistance of 316L SS substrates and Q_1 was the electrical double-layer capacitance at the substrate/electrolyte interface.

According to Table 5, BHP316L sample has an impedance modulus (|Z|) higher than 316L SS because of the protection ability of CaP coating. The charge transfer resistance through the macro-pores (R_{coat}) of the calcium phosphate film is higher than CaP film on stainless steel pretreated with H_2SO_4. This phenomenon occurs because the SS substrate forms a passive film at the bottom of the macropores when exposed to chloride ions, playing an important role in blocking corrosion [62]. Previous studies reported that 316L SS exhibits a passive behavior when exposed to H_2SO_4, which is due to the enrichment of Cr and Mo oxides in the surface layer that influences positively the localized corrosion resistance of 316L SS [18]. On the other hand, in this study the boiling acid H_2SO_4 media and porous nature of CaP coating on 1 M H_2SO_4 treated alloy may have contributed to the decline of the polarization resistance since CaP coating could not act as a mechanical barrier that avoids the penetration of chloride ions through the passive film, consequently leading to soluble corrosion product formation. In addition, from Table 5 it can be seen that the electrolyte resistance (R_s) of the T316L is lower than the P316L, which also corroborates to the found results, once a low resistance is generally associated with a high corrosion rate.

After implantation of a medical device or implant, an inflammatory response begins immediately in the human body, which will vary in terms of intensity and duration depending on the characteristics of the material and production of corrosion products [63]. Protein denaturation is a common method that can be correlated with an inflammatory response, while the inhibition of this response after the addition of a chemical component can be understood as an anti-inflammatory activity [64]. Due to the high concentration of albumin in human plasma (42 ± 3.5 $g{\cdot}L^{-1}$) [65], the interaction between albumin from chicken egg

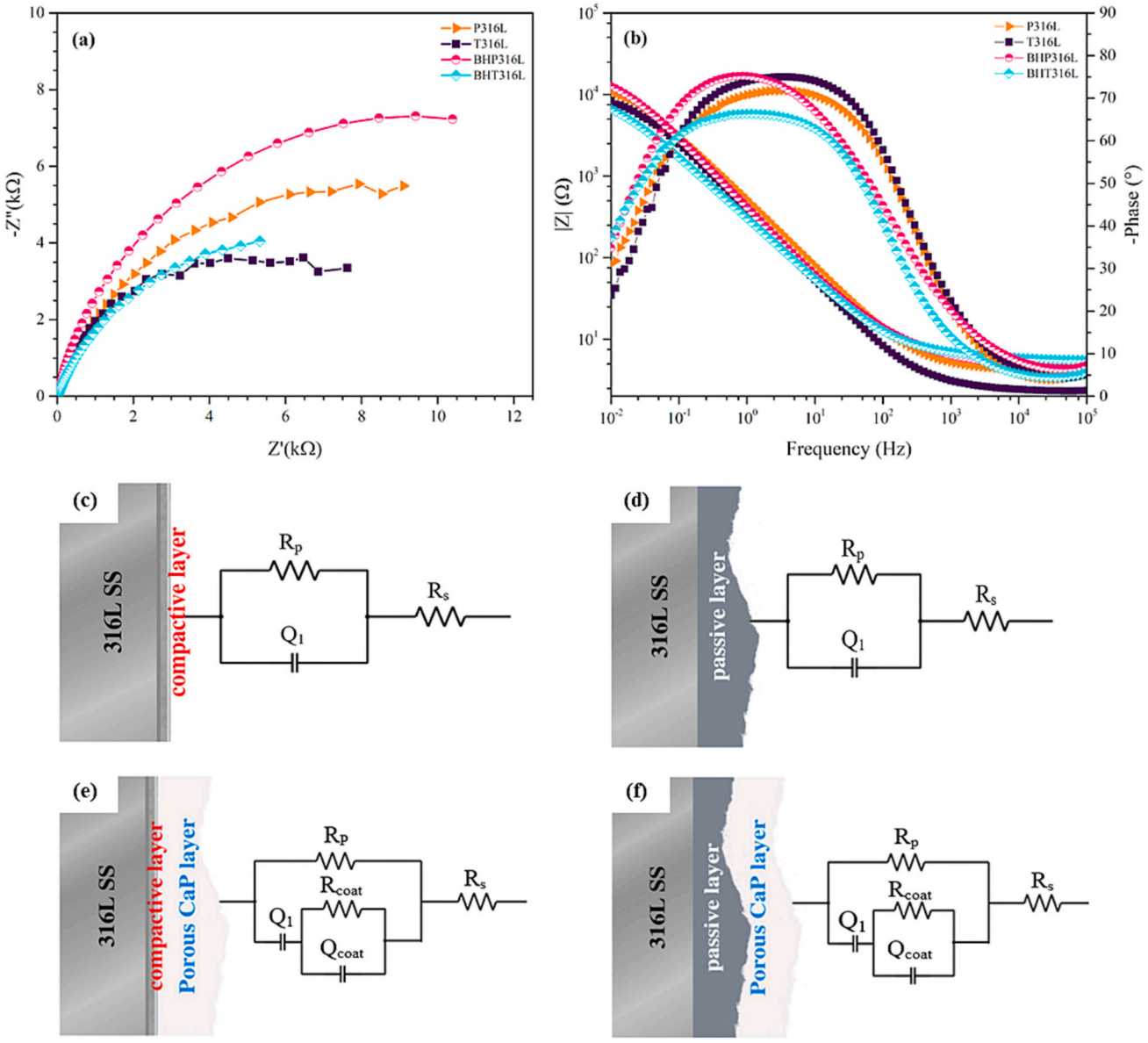

Fig. 6. Experimental EIS diagrams: a) Nyquist plot, b) Bode Modulus and Phase plots, and proposed equivalent circuit for modeling impedance parameters for the samples: c) P316L, d) T316L, e) BHP316L, and f) BHT316L.

Table 5
Impedance parameters for P316L, T316L, BHP316L, and BHT316L.

Parameters	P316L	T316L	BHP316L	BHT316L
R_s (Ω)	3.71 ± 0.77	2.53 ± 0.51	4.87 ± 0.87	5.89 ± 0.41
Q_{coat} (10^6 Ω s^{-n})	–	–	6.88 × 10^3 ± 2071.11	2.39 × 10^3 ± 67.18
n_2	–	–	0.50 ± 0.01	0.67 ± 0.10
Q_1 (10^6 Ω s^{-n})	470 ± 43.84	862.00 ± 438.41	588.14 ± 141.61	783.50 ± 14.85
n_1	0.81 ± 0.01	0.86 ± 0.02	0.81 ± 0.07	0.80 ± 0.02
R_{coat} (Ω) (porous)	–	–	5.659 ± 4.78	3.33 ± 0.12
R_1 (Ω) (barrier)	1.21 × 10^4 ± 3140.05	1.00 × 10^4 ± 856.31	1.76 × 10^4 ± 402.34	1.05 × 10^4 ± 711.35
Total impedance |Z| (Ω)	9.247 × 10^3 ± 1912.42	7.25 × 10^3 ± 706.81	1.27 × 10^4 ± 2729.85	6.69 × 10^3 ± 78.99

white and the coatings produced in this study becomes essential for the understanding of the anti-inflammatory activity. Fig. 8 shows the anti-inflammatory activity of BHP316L and BHT316L powders. Diclofenac sodium was used as a standard drug for absorbance. The BHP316L and diclofenac sodium samples follow an increasing concentration-dependent anti-inflammatory activity. It is observed that BHP316L is more effective in inhibiting inflammatory response than the BHT316L sample and from 400 μg mL^{-1} it has an anti-inflammatory activity superior to the drug used as reference. This result might be supported by the presence of particles measuring 21.3 nm in size discovered within the XRD analysis (Table 3). These particles size have been previously documented in literature to exhibit enhanced effectiveness. Meanwhile, the H_2SO_4 treated sample appears to increase protein denaturation, which may be related to the exposure of metal particles scraped off from the surface of passivated 316L SS. According to Zhang et al. [66], nickel leached from SS to surrounding tissues can inhibit cell proliferation and differentiation by altering the expression of related genes. Although the dissolution of nickel ions is low, the cytotoxicity of the corrosion product is relatively high as Fe and Cr ions are added to these complexes, which

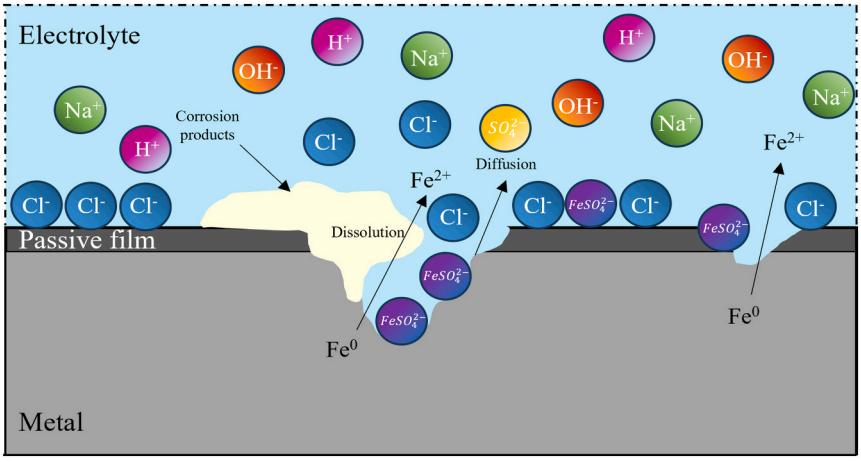

Fig. 7. Corrosion mechanism of 316L SS produced by sulfuric acid in the presence of chloride ions.

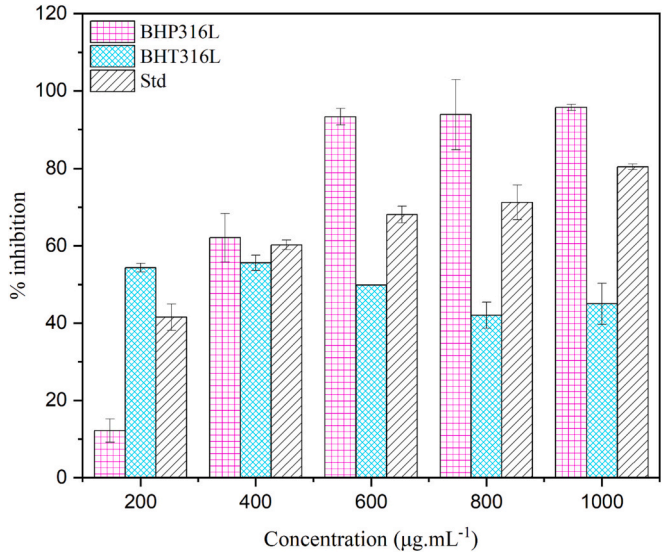

Fig. 8. Protein denaturation inhibition ability of BHP316L and BHT316L coatings.

are also toxic to cells. The complexes generated due to the interaction between albumin and metal ions can enter the circulation and cause side effects.

4. Conclusion

In this study, the impact of 1 M H_2SO_4 treatment at 70 °C before the electrodeposition process of calcium phosphate coating on 316L SS alloy was investigated. The SEM results revealed that the BHP316L coating consisted of irregular and non-uniform plate-like crystals while the BS/HAp coating on H_2SO_4 treated 316L SS possessed a uniformly distributed and regular shapes plate-like crystal structure. The EDS analysis showed a homogeneous distribution of Ca, P, and O overall surface ensuring a thorough CaP formation on the surface. The XRD confirmed the presence of two calcium phosphate phases (HAp and BS). From electrochemical studies, it was evidenced that BHT316L presented the lowest corrosion resistance in 0.9 % NaCl. This observation may be associated with low Mo concentration found by EDS analysis since molybdenum oxides are responsible for increased 316L SS resistance to localized corrosion attack. Powders scraped off from BHT316L coating increased protein denaturation, which may be related to the dissolution of toxic metallic complexes formed during the 316L SS treatment. Therefore, this work provides the potential to streamline coating processes and reduce associated costs by exploring alternative methods to improve the corrosion resistance of 316L SS and suggest that chemical modification may not always be necessary.

Supplementary data to this article can be found online at https://doi.org/10.1016/j.surfcoat.2023.130304.

CRediT authorship contribution statement

Gabriela Morais da Costa: Conceptualization, Data curation, Formal analysis, Investigation, Methodology, Project administration, Validation, Visualization, Writing – original draft, Writing – review & editing. **Gustavo Oliveira Everton:** Investigation, Methodology, Resources. **Gustavo Oliva Amaral:** Investigation, Writing – original draft. **Glauber Cruz:** Funding acquisition, Supervision, Writing – review & editing. **Anupama Ghosh:** Investigation, Methodology, Resources, Supervision, Validation, Visualization, Writing – original draft, Writing – review & editing. **Maria Eliziane Pires de Souza:** Conceptualization, Data curation, Formal analysis, Funding acquisition, Investigation, Methodology, Project administration, Resources, Software, Supervision, Validation, Visualization, Writing – original draft, Writing – review & editing.

Declaration of competing interest

The authors declare that they have no known competing financial interests or personal relationships that could have appeared to influence the work reported in this paper.

Data availability

Data will be made available on request.

Acknowledgments

The authors thank Aperam South America (Belo Horizonte, Brazil) for the donation of metallic materials (316L SS sheets) used in this work and for the financial support for this research from the National Council for Scientific and Technological Development (CNPq/PVCET2402-2020) and FAPEMA (Maranhão Foundation for Scientific Research and Technological Development - Processes no. 01661/21 and 06776/22). The authors are grateful to Analytical Centrals of the Federal University of Maranhão for the FT-IR analysis, (UFC/CTINFRA/MCTI-SISNANO/Pro-Equipamentos CAPES) for providing the Electron Scanning Microscopes (SEM images) and X-ray Laboratory at the Federal University of Ceará for XRD facilities (CNPq Grant number 402561/2007-4), Centro

Brasileiro de Pesquisas Físicas (Labnano/CBPF) where the cross sectional images analyzes were carried out, and Laboratório de Revestimentos Protetores for the profilometry analysis (Dr. Neileth Johanna Stand Figueroa).

References

[1] T.M. Sridhar, U. Kamachi Mudali, M. Subbaiyan, Preparation and characterisation of electrophoretically deposited hydroxyapatite coatings on type 316L stainless steel, Corros. Sci. 45 (2) (2003) 237–252.

[2] G. Blanda, V. Brucato, F.C. Pavia, S. Greco, S. Piazza, C. Sunseri, et al., Galvanic deposition and characterization of brushite/hydroxyapatite coatings on 316L stainless steel, Mater. Sci. Eng. C 64 (2016) 93–101, https://doi.org/10.1016/j.msec.2016.03.088 (Internet).

[3] M. Talha, C.K. Behera, O.P. Sinha, Potentiodynamic polarization study of Type 316L and 316LVM stainless steels for surgical implants in simulated body fluids, J. Chem. Pharm. Res. 4 (1) (2012) 203–208.

[4] W. Xu, F. Yu, L. Yang, B. Zhang, B. Hou, Y. Li, Accelerated corrosion of 316L stainless steel in simulated body fluids in the presence of H2O2 and albumin, Mater. Sci. Eng. C 92 (May) (2018) 11–19, https://doi.org/10.1016/j.msec.2018.06.023 (Internet).

[5] D. Cadosch, E. Chan, O.P. Gautschi, H.P. Simmen, L. Filgueira, Bio-corrosion of stainless steel by osteoclasts-in vitro evidence, J. Orthop. Res. 27 (7) (2009) 841–846.

[6] S. Kannan, A. Balamurugan, S. Rajeswari, H2SO4 as a passivating medium on the localised corrosion resistance of surgical 316L SS metallic implant and its effect on hydroxyapatite coatings, Electrochim. Acta 49 (15) (2004) 2395–2403.

[7] A. Motallebzadeh, N.S. Peighambardoust, S. Sheikh, H. Murakami, S. Guo, D. Canadinc, Microstructural, mechanical and electrochemical characterization of TiZrTaHfNb and Ti1.5ZrTa0.5Hf0.5Nb0.5 refractory high-entropy alloys for biomedical applications, Intermetallics 113 (April) (2019), 106572, https://doi.org/10.1016/j.intermet.2019.106572 (Internet).

[8] A. Asghari Alamdari, M. Hashemkhani, S. Hendessi, H. Yagci Acar, U. Unal, A. Motallebzadeh, A comprehensive study of microstructure, mechanical behavior, biocorrosion, and cytotoxicity of RF-PVD deposited Ti1.5ZrTa0.5Nb0.5X0.5 (X: Hf, Mo, and W) refractory high-entropy alloy films on 316L, Intermetallics 162 (June) (2023), 108003, https://doi.org/10.1016/j.intermet.2023.108003 (Internet).

[9] J. Fornell, Y.P. Feng, E. Pellicer, S. Suriñach, M.D. Baró, J. Sort, Mechanical behaviour of brushite and hydroxyapatite coatings electrodeposited on newly developed FeMnSiPd alloys, J. Alloys Compd. 729 (2017) 231–239.

[10] M. Kumar, J. Xie, K. Chittur, C. Riley, Transformation of modified brushite to hydroxyapatite in aqueous solution: effects of potassium substitution, Biomaterials 20 (15) (1999) 1389–1399.

[11] A. Haider, S. Haider, S.S. Han, I.K. Kang, Recent advances in the synthesis, functionalization and biomedical applications of hydroxyapatite: a review, RSC Adv. 7 (13) (2017) 7442–7458.

[12] Mir Saman Safavi, Frank C. Walsh, Maria A. Surmeneva RAS, JK-A, Electrodeposited hydroxyapatite-based biocoatings: recent progress and future challenges, Coatings 11 (1) (2021) 110.

[13] W. Wang, K.W.K. Yeung, Bone grafts and biomaterials substitutes for bone defect repair: a review, Bioact. Mater. 2 (4) (2017) 224–247, https://doi.org/10.1016/j.bioactmat.2017.05.007 (Internet).

[14] K.P. Ananth, J. Sun, J. Bai, An innovative approach to manganese-substituted hydroxyapatite coating on zinc oxide–coated 316L SS for implant application, Int. J. Mol. Sci. 19 (8) (2018).

[15] P. Kazimierczak, A. Przekora, Osteoconductive and osteoinductive surface modifications of biomaterials for bone regeneration: a concise review, Coatings 10 (2020) 971.

[16] V.K. Balla, M. Das, S. Bose, G.D. Janaki Ram, I. Manna, Laser surface modification of 316 L stainless steel with bioactive hydroxyapatite, Mater. Sci. Eng. C 33 (8) (2013) 4594–4598, https://doi.org/10.1016/j.msec.2013.07.015 (Internet).

[17] S. Kannan, A. Balamurugan, S. Rajeswari, Hydroxyapatite coatings on sulfuric acid treated type 316L SS and its electrochemical behaviour in Ringer's solution, Mater. Lett. 57 (16–17) (2003) 2382–2389.

[18] A. Parsapour, S.N. Khorasani, M.H. Fathi, Corrosion behavior and biocompatibility of hydroxyapatite coating on H 2SO4 passivated 316L SS for human body implant, Acta Metall. Sin. (English Lett.) 26 (4) (2013) 409–415.

[19] J.A. Moreto, R.V. Gelamo, M.V. da Silva, T.T. Steffen, C.J.F. de Oliveira, P.A. de Almeida Buranello, et al., New insights of Nb2O5-based coatings on the 316L SS surfaces: enhanced biological responses, J. Mater. Sci. Mater. Med. 32 (3) (2021) 2–7, https://doi.org/10.1007/s10856-021-06498-7 (Internet).

[20] D.T.M. Thanh, P.T. Nam, N.T. Phuong, L.X. Que, Anh N. Van, T. Hoang, et al., Controlling the electrodeposition, morphology and structure of hydroxyapatite coating on 316L stainless steel, Mater. Sci. Eng. C 33 (4) (2013) 2037–2045, https://doi.org/10.1016/j.msec.2013.01.018 (Internet).

[21] D. Gopi, V.C.A. Prakash, L. Kavitha, Evaluation of hydroxyapatite coatings on borate passivated 316L SS in Ringer's solution, Mater. Sci. Eng. C 29 (3) (2009) 955–958, https://doi.org/10.1016/j.msec.2008.08.020 (Internet).

[22] N. Eliaz, T.M. Sridhar, U.K. Mudali, B. Raj, Electrochemical and electrophoretic deposition of hydroxyapatite for orthopaedic applications, Surf. Eng. 21 (3) (2005) 238–242.

[23] P.T. Nam, N.T. Thom, N.T. Phuong, V.T. Hanh, N.T.T. Trang, V.T.H. Van, et al., Electrodeposition of sustainable fluoridated hydroxyapatite coatings on 316L stainless steel for application in bone implant, Green Process Synth. 5 (5) (2016) 499–510.

[24] L. Benea, E. Mardare-Danaila, M. Mardare, J.P. Celis, Preparation of titanium oxide and hydroxyapatite on Ti-6Al-4V alloy surface and electrochemical behaviour in bio-simulated fluid solution, Corros. Sci. 80 (2014) 331–338, https://doi.org/10.1016/j.corsci.2013.11.059 (Internet).

[25] A. Jenifer, K. Senthilarasan, S. Arumugam, P. Sivaprakash, S. Sagadevan, P. Sakthivel, Investigation on antibacterial and hemolytic properties of magnesium-doped hydroxyapatite nanocomposite, Chem. Phys. Lett. 771 (March) (2021), 138539, https://doi.org/10.1016/j.cplett.2021.138539 (Internet).

[26] S.J. Kalita, S. Verma, Nanocrystalline hydroxyapatite bioceramic using microwave radiation: synthesis and characterization, Mater. Sci. Eng. C 30 (2) (2010) 295–303, https://doi.org/10.1016/j.msec.2009.11.007 (Internet).

[27] N. Rameshbabu, T.S. Sampath Kumar, Rao K. Prasad, Synthesis of nanocrystalline fluorinated hydroxyapatite by microwave processing and its in vitro dissolution study, Bull. Mater. Sci. 29 (6) (2006) 611–615.

[28] H. Nosrati, D.Q.S. Le, R.Z. Emamehc, M.C. Perez, C.E. Bünger, Nucleation and growth of brushite crystals on the graphene sheets applicable in bone cement, Bol la Soc Esp Ceram y Vidr 61 (1) (2022) 27–34, https://doi.org/10.1016/j.bsecv.2020.05.001 (Internet).

[29] T.N. Pham, T.M.T. Dinh, T.T. Nguyen, T.P. Nguyen, E. Kergourlay, D. Grossin, et al., Operating parameters effect on physicochemical characteristics of nanocrystalline apatite coatings electrodeposited on 316L stainless steel, Adv. Nat. Sci. Nanosci. Nanotechnol. 8 (3) (2017).

[30] A. Rogina, M. Ivanković, H. Ivanković, Preparation and characterization of nano-hydroxyapatite within chitosan matrix, Mater. Sci. Eng. C 33 (8) (2013) 4539–4544.

[31] Z. Peng, W. Xu, Y. Liu, K. Zhao, P. Hu, Anisotropy evaluation and defect detection on laser power bed fusion 316L stainless steel, Micromachines 14 (6) (2023).

[32] D. Sivaraj, K. Vijayalakshmi, Novel synthesis of bioactive hydroxyapatite/f-multiwalled carbon nanotube composite coating on 316L SS implant for substantial corrosion resistance and antibacterial activity, J. Alloys Compd. 777 (2019) 1340–1346, https://doi.org/10.1016/j.jallcom.2018.10.341 (Internet).

[33] N. Ribeiro, S.R. Sousa, F.J. Monteiro, Influence of crystallite size of nanophased hydroxyapatite on fibronectin and osteonectin adsorption and on MC3T3-E1 osteoblast adhesion and morphology, J. Colloid Interface Sci. 351 (2) (2010) 398–406, https://doi.org/10.1016/j.jcis.2010.08.013 (Internet).

[34] Y. Cai, Y. Liu, W. Yan, Q. Hu, J. Tao, M. Zhang, et al., Role of hydroxyapatite nanoparticle size in bone cell proliferation, J. Mater. Chem. 17 (36) (2007) 3780–3787.

[35] Z. Shi, X. Huang, Y. Cai, R. Tang, D. Yang, Size effect of hydroxyapatite nanoparticles on proliferation and apoptosis of osteoblast-like cells, Acta Biomater. 5 (1) (2009) 338–345, https://doi.org/10.1016/j.actbio.2008.07.023 (Internet).

[36] J.L. Xu, K.A. Khor, J.J. Sui, J.H. Zhang, W.N. Chen, Protein expression profiles in osteoblasts in response to differentially shaped hydroxyapatite nanoparticles, Biomaterials 30 (29) (2009) 5385–5391, https://doi.org/10.1016/j.biomaterials.2009.07.002 (Internet).

[37] F. Yang, J.G.C. Wolke, J.A. Jansen, Biomimetic calcium phosphate coating on electrospun poly(ε-caprolactone) scaffolds for bone tissue engineering, Chem. Eng. J. 137 (1) (2008) 154–161.

[38] V.P. Feitosa, M.G. Bazzocchi, A. Putignano, G. Orsini, A.L. Luzi, M.A.C. Sinhoreti, et al., Dicalcium phosphate (CaHPO4·2H2O) precipitation through ortho- or meta-phosphoric acid-etching: effects on the durability and nanoleakage/ultra-morphology of resin-dentine interfaces, J. Dent. 41 (11) (2013) 1068–1080.

[39] A.A. Shaltout, M.A. Allam, M.A. Moharram, FTIR spectroscopic, thermal and XRD characterization of hydroxyapatite from new natural sources, Spectrochim. Acta Part A Mol. Biomol. Spectrosc. 83 (1) (2011) 56–60, https://doi.org/10.1016/j.saa.2011.07.036 (Internet).

[40] L.T. Bang, B.D. Long, R. Othman, Carbonate hydroxyapatite and silicon-substituted carbonate hydroxyapatite: synthesis, mechanical properties, and solubility evaluations, Sci. World J. 2014 (2014).

[41] D. Gopi, V. Collins Arun Prakash, L. Kavitha, S. Kannan, P.R. Bhalaji, E. Shinyjoy, et al., A facile electrodeposition of hydroxyapatite onto borate passivated surgical grade stainless steel, Corros. Sci. 53 (6) (2011) 2328–2334, https://doi.org/10.1016/j.corsci.2011.03.018 (Internet).

[42] S. Arul Xavier, U. Vijayalakshmi, Electrochemically grown functionalized-multi-walled carbon nanotubes/hydroxyapatite hybrids on surgical grade 316L SS with enhanced corrosion resistance and bioactivity, Colloids Surf. B: Biointerfaces 171 (May) (2018) 186–196.

[43] D.M. Liu, Q. Yang, T. Troczynski, Sol-gel hydroxyapatite coatings on stainless steel substrates, Biomaterials 23 (3) (2002) 691–698.

[44] F. Bir, H. Khireddine, D. Ksouri, H. Benhayoune, A. Maho, Characterization of HA/FHA coatings on smooth and rough implant surface by pulsed electrodeposition, Int. J. Appl. Ceram. Technol. 12 (2015) E222–E234.

[45] T.T. Li, L. Ling, M.C. Lin, H.K. Peng, H.T. Ren, C.W. Lou, et al., Recent advances in multifunctional hydroxyapatite coating by electrochemical deposition, J. Mater. Sci. 55 (15) (2020) 6352–6374, https://doi.org/10.1007/s10853-020-04467-z (Internet).

[46] M.H. Fathi, M. Salehi, A. Saatchi, V. Mortazavi, S.B. Moosavi, In vitro corrosion behavior of bioceramic, metallic, and bioceramic-metallic coated stainless steel dental implants, Dent. Mater. 19 (3) (2003) 188–198.

[47] R. Subramani, S. Elangomannan, K. Louis, S. Kannan, D. Gopi, Fabrication of minerals substituted porous hydroxyapaptite/poly(3,4-ethylenedioxy pyrrole-co-3,4-ethylenedioxythiophene) bilayer coatings on surgical grade stainless steel and its antibacterial and biological activities for orthopedic applications, ACS Appl. Mater. Interfaces 8 (19) (2016) 12404–12421.

[48] E.A. Abdel-Aal, D. Dietrich, S. Steinhaeuser, B. Wielage, Electrocrystallization of nanocrystallite calcium phosphate coatings on titanium substrate at different current densities, Surf. Coat. Technol. 202 (24) (2008) 5895–5900.
[49] T.T. Thanh, C.M. Cotrut, M.D. Vranceanu, E. Ungureanu, M. Tarcolea, Studies of microstructure and composition of modified hydroxyapatite coatings via sem investigations, UPB Sci. Bull. Ser. B Chem. Mater. Sci. 82 (1) (2020) 145–154.
[50] Z. Cao, L. Li, L. Yang, L.L. Yao, H. Wang, X. Yu, et al., Osteoinduction evaluation of fluorinated hydroxyapatite and tantalum composite coatings on magnesium alloys, Front. Chem. 9 (September) (2021) 1–11.
[51] M. Assadian, H. Jafari, S.M. Ghaffari Shahri, M.H. Idris, B. Gholampour, Corrosion resistance of EPD nanohydroxyapatite coated 316L stainless steel, Surf. Eng. 30 (11) (2014) 806–813.
[52] N. Eliaz, O. Ritman-Hertz, D. Aronov, E. Weinberg, Y. Shenhar, G. Rosenman, et al., The effect of surface treatments on the adhesion of electrochemically deposited hydroxyapatite coating to titanium and on its interaction with cells and bacteria, J. Mater. Sci. Mater. Med. 22 (7) (2011) 1741–1752.
[53] R. Drevet, H. Benhayoune, Electrodeposition of calcium phosphate coatings on metallic substrates for bone implant applications: a review, Coatings 12 (4) (2022).
[54] R. Ahmadi, A. Afshar, In vitro study: bond strength, electrochemical and biocompatibility evaluations of TiO2/Al2O3 reinforced hydroxyapatite sol–gel coatings on 316L SS, Surf. Coat. Technol. 405 (2021), 126594, https://doi.org/10.1016/j.surfcoat.2020.126594 (Internet, October 2020).
[55] L. Xu, Y. Zuo, J. Tang, Y. Tang, P. Ju, Chromium-palladium films on 316L stainless steel by pulse electrodeposition and their corrosion resistance in hot sulfuric acid solutions, Corros. Sci. 53 (11) (2011) 3788–3795, https://doi.org/10.1016/j.corsci.2011.07.029 (Internet).
[56] R.C.C. Rangel, M.E.P. Souza, W.H. Schreiner, C.M.A. Freire, E.C. Rangel, N.C. Cruz, Effect of the fluorination of DLC film on the corrosion protection of aluminum alloy (AA 5052), Surf. Coat. Technol. 204 (18–19) (2010) 3022–3028, https://doi.org/10.1016/j.surfcoat.2010.03.055 (Internet).
[57] J. Jomy, S. Sharma, P.R. Prabhu, D. Prabhu, Corrosion behavior of EN18 steel and copper in the sulfuric acid medium for as-bought and annealed materials, J. Mater. Eng. Perform. 32 (18) (2023) 8247–8261, https://doi.org/10.1007/s11665-022-07698-0 (Internet).
[58] A.H. Al-Moubaraki, A.A. Ganash, S.D. Al-Malwi, Investigation of the corrosion behavior of mild steel/H2SO4 systems, Moroccan J. Chem. 8 (1) (2020) 264–279.
[59] S. Gudić, L. Vrsalović, A. Matošin, J. Krolo, E.E. Oguzie, A. Nagode, Corrosion behavior of stainless steel in seawater in the presence of sulfide, Appl. Sci. 13 (7) (2023).
[60] S. Zheng, C. Li, Y. Qi, L. Chen, C. Chen, Mechanism of (Mg,Al,Ca)-oxide inclusion-induced pitting corrosion in 316L stainless steel exposed to sulphur environments containing chloride ion, Corros. Sci. 67 (2013) 20–31, https://doi.org/10.1016/j.corsci.2012.09.044 (Internet).
[61] Y. Xiao, J. Tang, Y. Wang, B. Lin, Z. Nie, Y. Li, et al., Corrosion behavior of 2205 duplex stainless steel in NaCl solutions containing sulfide ions, Corros. Sci. 200 (2022), 110240, https://doi.org/10.1016/j.corsci.2022.110240 (Internet, June 2021).
[62] J. Tang, Z. Zhang, Y. Wang, P. Ju, Y. Tang, Y. Zuo, Corrosion resistance mechanism of palladium film-plated stainless steel in boiling H2SO4 solution, Corros. Sci. 135 (February) (2018) 222–232, https://doi.org/10.1016/j.corsci.2018.02.055 (Internet).
[63] J.M.A. Jiang, S., The immune response to implanted materials and devices: the impact of the immune system on the success of an implant, in: Immune Response to Implant Mater Devices Impact Immune Syst Success an Implant, 2016, pp. 15–36.
[64] O. Antonoglou, K. Lafazanis, S. Mourdikoudis, G. Vourlias, T. Lialiaris, A. Pantazaki, et al., Biological relevance of CuFeO 2 nanoparticles: antibacterial and anti-inflammatory activity, genotoxicity, DNA and protein interactions, Mater. Sci. Eng. C 99 (2019) 264–274 (September 2018).
[65] Y.S. Hedberg, M.S. Killian, E. Blomberg, S. Virtanen, P. Schmuki, Wallinder I. Odnevall, Interaction of bovine serum albumin and lysozyme with stainless steel studied by time-of-flight secondary ion mass spectrometry and X-ray photoelectron spectroscopy, Langmuir 28 (47) (2012) 16306–16317.
[66] C. Zhang, L. He, Y. Chen, D. Dai, Y. Su, L. Shao, Corrosion behavior and in vitro cytotoxicity of Ni-Ti and stainless steel arch wires exposed to lysozyme, ovalbumin, and bovine serum albumin, ACS Omega 5 (30) (2020) 18995–19003.